**ARTICLE**

Check for updates

Multifunctional Integrated Organic–Inorganic-Metal Hybrid Aerogel for Excellent Thermal Insulation and Electromagnetic Shielding Performance

Zhaoqi Niu[1], Fengjin Qu[2,3], Fang Chen[1], Xiaoyan Ma[1] ✉, Beixi Chen[1], Luyao Wang[1], Miao Xu[1], Shumeng Wang[1], Liang Jin[4], Chengshuang Zhang[5], Xiao Hou[1,6] ✉

HIGHLIGHTS

- The homogeneous hybridization of organic–inorganic-metal elements in 3D aerogel was achieved by an expeditious method.

- The aerogel tightly integrates excellent thermal insulation (49.6 mW m^{-1} K^{-1}), ablative resistance, mechanical strength, and super-hydrophobic properties.

- The ablated carbon aerogel combines notable electromagnetic interference shielding properties (31.6 dB) and load-carrying properties (272.8 kN·m kg^{-1}).

ABSTRACT Vehicles operating in space need to withstand extreme thermal and electromagnetic environments in light of the burgeoning of space science and technology. It is imperatively desired to high insulation materials with lightweight and extensive mechanical properties. Herein, a boron–silica–tantalum ternary hybrid phenolic aerogel (BSiTa-PA) with exceptional thermal stability, extensive mechanical strength, low thermal conductivity (49.6 mW m^{-1} K^{-1}), and heightened ablative resistance is prepared by an expeditious method. After extremely thermal erosion, the obtained carbon aerogel demonstrates noteworthy electromagnetic interference (EMI) shielding performance with an efficiency of 31.6 dB, accompanied by notable loading property with specific modulus of 272.8 kN·m kg^{-1}. This novel design concept has laid the foundation for the development of insulation materials in more complex extreme environments.
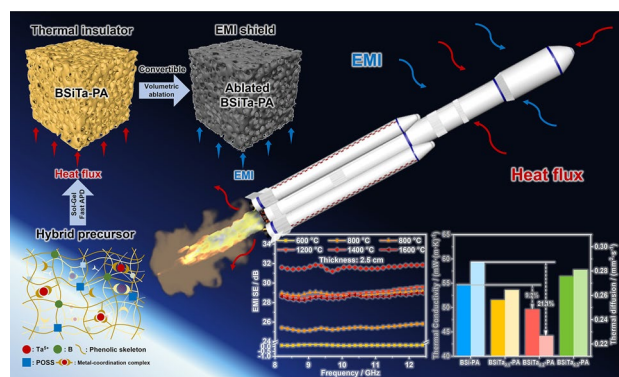
✉ Xiaoyan Ma, m_xiao_yana@nwpu.edu.cn; Xiao Hou, houxiaoht@163.com

[1] Ministry of Industry and Information Technology Key Laboratory of Special Function and Smart Polymer Materials, Key Laboratory of Materials Physics and Chemistry of Ministry of Education for Extraordinary Conditions, Northwestern Polytechnical University, Xi'an 710072, People's Republic of China

[2] Spallation Neutron Source Science Center Institution, Dongguan 523803, People's Republic of China

[3] Institute of High Energy Physics, Chinese Academy of Sciences, Beijing 100049, People's Republic of China

[4] China Aerospace Science and Industry Corporation Sixth Academy, Hohhot 022185, People's Republic of China

[5] Xi'an Aerospace Composites Research Institute, Xi'an 710025, People's Republic of China

[6] China Aerospace Science and Technology Corporation, Beijing 100037, People's Republic of China

Springer

1 Introduction

The expanding demands of launch vehicles have promoted the booming development of high-performance lightweight functional materials [1–3]. Aerogels, due to its exceptional low density and insulating capabilities, are in expanding demands in the field of space vehicles [4–8]. In the practical applications, space vehicles not only need to withstand the extreme heat erosion, but also need to block electromagnetic interference from cosmic space [8–12]. However, due to separate performance-oriented material design, there are few reports of compatibility and integration of these two features.

As a representative of organic aerogel, phenolic aerogel possesses excellent thermal stability and high-temperature shape retention rate upon traditional organic aerogel, which has been applied in the field of aerospace thermal insulation [13–15]. For thermal protection-oriented aerogels, serious carbonization and ceramization usually occur during the extremely thermal protection process [16]. Coincidentally, for EMI shielding aerogels, their properties are affected by the material's intrinsic chemical structure, porous structure, degree of graphitization, and electrical conductivity [17]. Accordingly, to fit the advancement of multifunctional aerospace materials, an interesting strategy is proposed to develop a convertible aerogel that can transform into an EMI shield after undergoing extreme thermal environmental ablation, which will not only enable the integration of performance, but also the full utilization of the material. For the convertible strategy, the carbonization capacity is crucial for its convertible performance. Studies have shown that covalently bonded inorganic and metal hybrid elements have positive effects on the thermal stability and ablative resistance performance improvement of phenolic resin, because the hybrid elements endow a more stable chemical structure and can delay the pyrolysis process of the resin with forming carbon/ceramic structure to withstand the heat flow erosion [18, 19].

Recently, the reported modified phenolic aerogels usually comprise only one or two functional elements, lacking the further integration and development of functional features [20, 21]. The hybrid phenolic precursor containing three or more functional elements and its three-dimensional aerogel,

however, has not been reported, owing to the difficulties for material preparation: (i) The utilization of modifiers needs to consider not only the amount and type of reactive sites in the chemical structure of the phenolic resin to meet the requirements of the chemical reaction during the modification process, but also the reaction between the modifier and the phenolic resin, which will affect its molding process and material properties; (ii) hybrid phenolic resin precursor solutions exhibit strong intramolecular and intermolecular non-covalent interactions, especially π stacking, hydrogen bonding and coordination, leading to a rapid phase separation and co-precipitation of hybrid phenolic sol rather than the formation of a uniform gel network due to this unstable sol–gel process. Therefore, the uniform integration of multiple hybrid elements as inorganic and metal components into 3D high-performance hybrid aerogels is a major challenge.

Here, we report the development of organic–inorganic-metal hybrid aerogel with convertible features and multifunctional properties. The hybrid aerogels are obtained by sol–gel preparation of Ta^{5+}-chelated boron–silicon phenolic resin (catalyzed by polyhedral oligomeric silsesquioxanes (POSS)), followed by rapid ambient pressure drying (APD) process. Tantalum has excellent high temperature resistance, and the TaC formed by high-temperature ablation possesses both excellent electrical conductivity and high melting point, which not only is a key for its thermal insulation, but also the guarantee to its EMI shielding efficiency. Thanks to the performance gains by selected functional elements, the resulting hybrid aerogel exhibits low density, excellent thermal stability, mechanical strength, thermal insulation, and ablative resistance. After volumetric ablation, the hybrid aerogel turns to be a carbon aerogel, possessing good ceramization, electrical conductivity, and multi-scale micro-/ nanopore structure, presenting a good EMI performance. To deeply understand the structure–performance relationship of the hybrid aerogel, we investigated the microstructure evolution of the hybrid aerogel pyrolyzed at different ablated temperatures. The crystal structure evolution of carbon and ceramic was analyzed by X-ray diffraction (XRD), X-ray photoelectron spectroscopy (XPS), and Raman spectroscopy. Meanwhile, small-angle X-ray scattering (SAXS) and mercury intrusion porosimetry (MIP) were adopted to analyze the nano-micron pore structure of the ablated

carbon aerogel. This work demonstrates the feasibility of the proposed design concept and the great potential of multicomponent hybrid aerogel as a lightweight and promising multifunctional material.

2 Experimental Section

2.1 Materials

The *p*-toluenesulfonic acid, ethanol–tantalum, and anhydrous ethanol were purchased from Aladdin Biochemical Technology Co., Ltd. (Shanghai, China). The boron–silica hybrid phenolic resin catalyzed by POSS was synthesized according our previously report [18]. All chemicals were used without further purification.

2.2 Preparation of Boron–Silica–Tantalum Hybrid Phenolic Aerogel and Carbon Aerogel

The entire preparation procedure of the boron–silicon–tantalum ternary hybrid phenolic aerogel (BSiTa-PA) is shown in Fig. 1. The boron–silica–tantalum hybrid phenolic aerogel was prepared by covalent and coordination hybridization, accompanied by sol–gel and fast APD process. Specifically, 15 g of the boron–silica hybrid phenolic resin was dissolved in 80 g of anhydrous ethanol to obtain a 15.8 wt% resin solution. Afterward, 0.03 g of ethanol–tantalum was added to 20 g of anhydrous ethanol and stirred to obtain a homogeneous solution. The resin solution of 15.8 wt% was slowly added to the above ethanol–tantalum ethanol solution and stirred evenly to obtain the boron–silica–tantalum homogeneous hybrid resin precursor solution. During the coordination process, $Ta(OC_2H_5)_5$ rapidly initiated self-assembly with the hybrid phenolic resin, upon diffusion into the boron–silica hybrid phenolic resin solution. Then, 0.75 g of *p*-toluenesulfonic acid was added into the boron–silica–tantalum hybrid resin precursor solution as a catalyst and stirred evenly. Finally, the hybrid aerogel was prepared by a simple high-pressure assisted polymerization combined with fast APD process. The aging process of sol–gel and gel was completed by placing the resin solution in an autoclave at 180 °C for 24 h. Once the ambient temperature reached the polycondensation temperature of hybrid precursor, the hybrid precursor promptly cross-linked and separated from the solvent
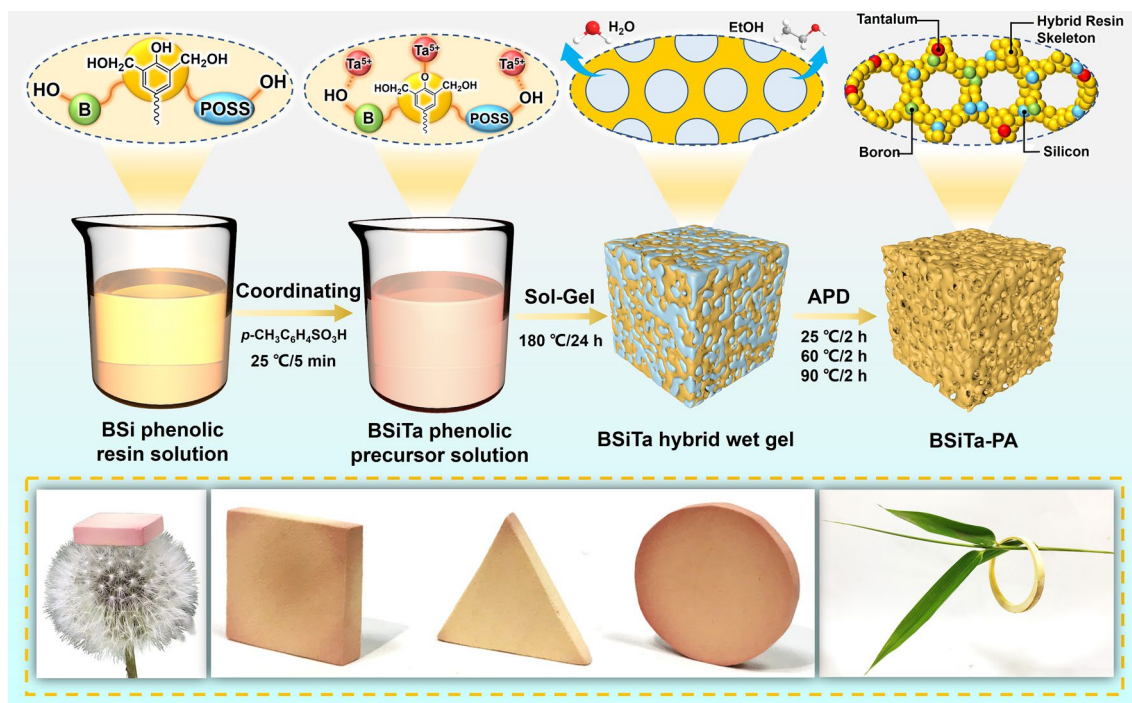
Fig. 1 Schematic description of the multifunctional aerogel preparation process and photographs (bottom) of the aerogel with different geometric shapes

phase to form a uniform hybrid wet gel, containing B, Si, and Ta. The gel was removed without solvent exchange and dried at atmospheric pressure for 6 h to replace the solvent and air inside the gel. The product was named $BSiTa_{0.2}$-PA. Other samples were prepared by changing the concentration of ethanol–tantalum. The concentration of the precursors (resin and *p*-toluenesulfonic acid) remains constant and is indicated by the ratio of the weight of the precursors to the weight of the sol. The hybrid aerogel without tantalum was named BSi-PA, and the tantalum hybrid aerogel was named $BSiTa_x$-PA ($x = 0.1, 0.2, 0.3$, where x indicates the trend of the amount of ethanol-tantalum).

$BSiTa_{0.2}$-PA was placed in a tube furnace protected by Ar atmosphere and heated at a rate of 10 °C min^{-1} to 600, 800, 1000, 1200, 1400, and 1600 °C, respectively, and kept at each temperature point for 1 h. After cooling to room temperature at the same rate, the aerogels produced by volumetric ablation at different temperatures can be obtained.

3 Results and Discussion

3.1 Preparation and Microstructure of BSiTa-PA

The Fourier transform infrared spectrometer spectra of the as-prepared B, Si, and Ta hybrid resin and the B, Si hybrid resin without Ta^{5+} as reference are displayed in Fig. S1a. It is evident that $Ta(OC_2H_5)_5$ addition greatly lowers the hydroxyl peak and the peak shifts from 3253 to 3307 cm^{-1}, indicating that Ta^{5+} is coordinated to form a stable chelated structure [22]. In addition, the results of thermogravimetric analysis (TGA) and derivative thermogravimetric (DTG) curves of the cured hybrid resins in Fig. S2b, c show that the hybrid resins possess advanced thermal stability, and the pyrolysis trend of the $BSiTa_{0.2}$ hybrid resin in the initial decomposition stage (< 600 °C) is completely different from that of the BSi hybrid resin, with the thermal decomposition significantly delayed. At this stage, the reason of decomposition is mainly due to the dehydration of hydroxyl groups, etc., and thus this also indirectly proves the successful coordination of Ta^{5+}. The chemical structure analysis of $BSiTa_{0.2}$-PA by XPS is shown in Fig. S2d–f, in which B, Si and Ta^{5+} are all bonded to the organic skeleton of phenolic aerogel through covalent and coordination bonds. The $BSiTa_x$-PA hybrid aerogel monoliths are amenable to

subtractive manufacturing processes, enabling the creation of a variety of desired shapes, including cuboids, tri-prisms, cylinders, and rings.

The microscopic morphological characteristics of the prepared phenolic aerogels are presented in Fig. 2. The scanning electron microscope (SEM) images showed that the aerogel network was composed of primary nanoparticles and submicron clusters, and all aerogels showed similar three-dimensional thick neck micro-nano-network structure, which was different from the traditional thin neck "pearl necklace" network structure of inorganic aerogels, which may indirectly indicate that the aerogel possesses better mechanical strength (Fig. 2a–d); meanwhile, according to the Young–Laplace equation (Eq. S1), the existence of macro-scale pores observed from SEM images is one of the necessary conditions for successful APD process, which can effectively reduce the capillary force and avoid the collapse of the gel structure [6].

Since there are many macro-scale pores in aerogel, the MIP was used to further analyze the microscopic features of the pores, as shown in Fig. 2e–h, S4 and Table S2. With the addition of $Ta(OC_2H_5)_5$, the secondary particles with the size of tens of nanometers tend to form finer microstructure, while the specific surface area and average pore size of macro-scale pores of aerogel are also affected by the Ta^{5+} content. The results show that the pore specific surface area is 33.3–44.2 m^2 g^{-1}, of which the maximum value is 44.2 m^2 g^{-1} of $BSiTa_{0.2}$-PA, and the average pore diameter of macroscopic scale is 2.4–6.7 µm, of which the minimum is 2.4 µm of $BSiTa_{0.2}$-PA. This transformation may be due to the rapid self-assembly between hybrid phenolic precursor and Ta^{5+} with appropriate content to form more stable chelated macromolecules.

Therefore, as a representative, the microstructure of the $BSiTa_{0.2}$-PA aerogel hybrid domain was further examined by high-resolution transmission electron microscopy (HRTEM) and energy-dispersive X-ray spectroscopy (EDS) element mapping shown in Fig. 2i. It was found that the hybrid skeleton structure composed by organic phenolic resin and boron, silicon, and tantalum hybrid elements have continuous amorphous phases. The element mapping images confirmed the uniform distribution of silicon, boron, and tantalum components in the aerogel skeleton, which was attributed to the ethanol-stabilized hybrid phenolic heat-induced sol–gel rapid phase separation process.
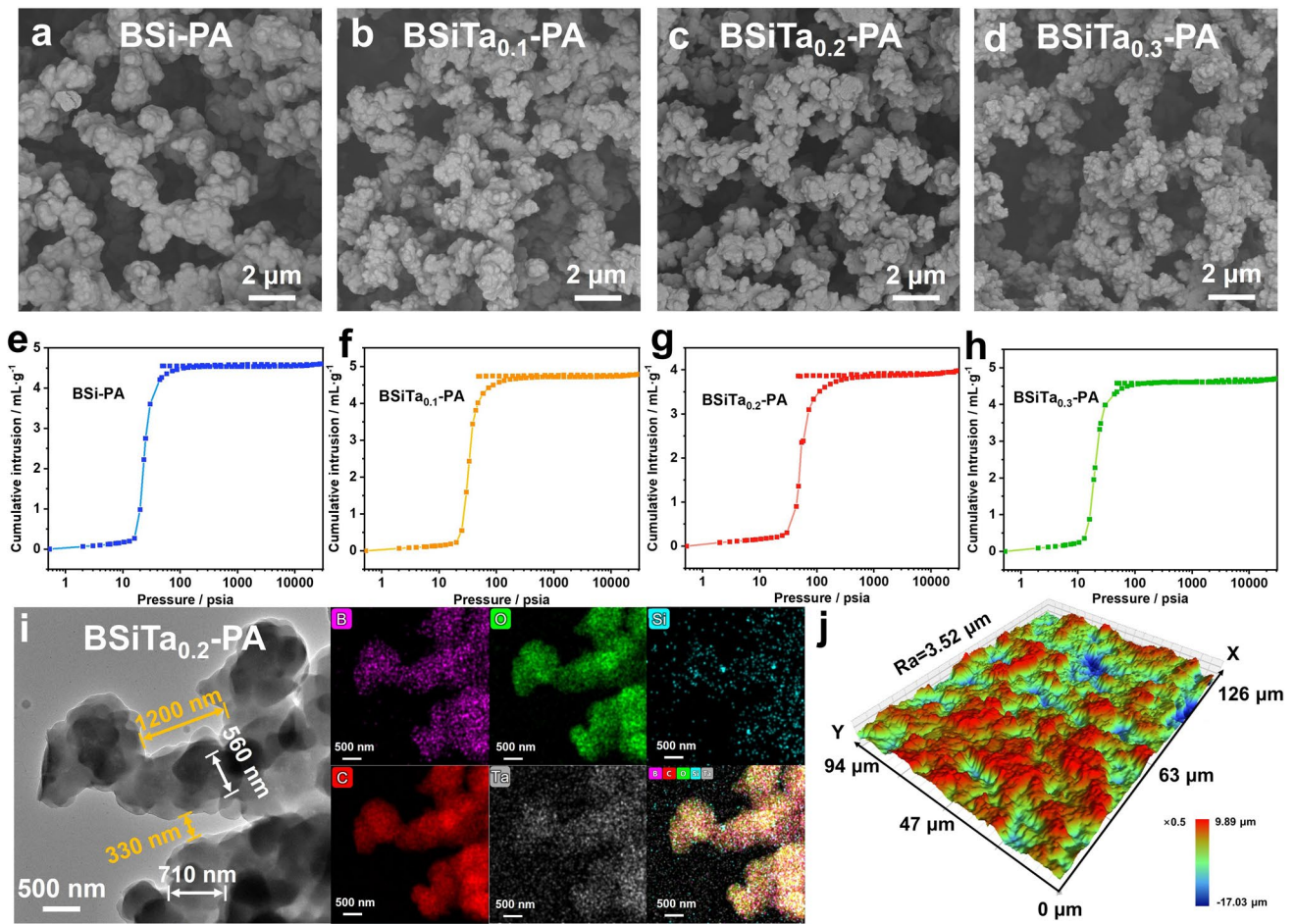
Fig. 2 Morphological and structural characteristics of BSi-PA and BSiTa-PA aerogels. **a-d** SEM images of fracture surface of the aerogels with different Ta^{5+} contents, **e–h** intrusion and extrusion curves of mercury and the attaching pore size distributions. **i** HRTEM and elemental mapping images show the nanostructure and the homogeneous distribution of the hybrid element domain. **j** Laser optical 3D surface image of the $BSiTa_{0.2}$-PA

The surface morphology of hybrid aerogel was studied by laser optical 3D imaging, as shown in Figs. 2j and S3. The roughness of BSi-PA aerogel is 2.88 μm, whereas it is 3.52 μm in $BSiTa_{0.2}$-PA aerogel. The increase of surface roughness may significantly improve the hydrophobic properties of the aerogel, as is shown in Supporting Information.

3.2 Thermal Stability, Mechanical Property, and Thermal Insulation Performance of BSiTa-PA

As an advanced thermal protection material, aerogel's thermal insulation and ablative resistance performances

are of vital importance [23–26]. Specifically, thermal stability is a significant factor for ablative resistance [27–31]. As shown in Fig. 3a, with the increase of Ta^{5+} content, the thermal stability of the aerogels displays the tendency of rising up at the beginning and then declining in late. The initial decomposition temperature ($T_{5\%}$ and $T_{10\%}$, representing the temperature corresponding to 5 and 10 wt% decomposition) of $BSiTa_{0.2}$-PA is 158.9 and 200.3 °C higher than those of BSi-PA, respectively, and the char yield at 1000 °C of $BSiTa_{0.2}$-PA is 4.5% higher than that of BSi-PA, indicating the aerogel with appropriate Ta^{5+} possess better thermal stability. The thermal stability of
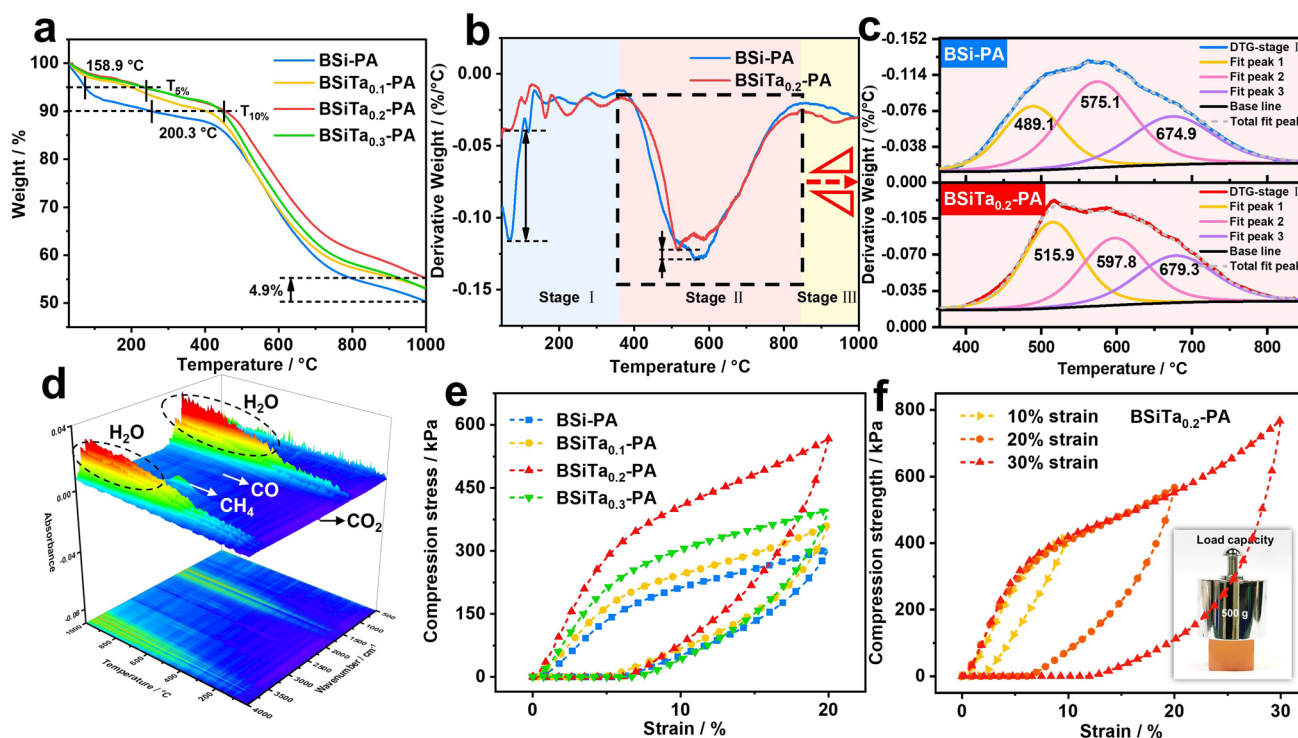
Fig. 3 Thermal stability properties: **a-b** TGA and DTG curves of hybrid aerogels, **c** the deconvoluted peaks of DTG stage II, **d** three-dimensional mapping TG-IR diagram of volatile product for $BSiTa_{0.2}$-PA. Mechanical properties: **e** $\sigma-\varepsilon$ curves of BSi-PA and BSiTa-PA aerogels under 20% ε, **f** $\sigma-\varepsilon$ curves of $BSiTa_{0.2}$-PA aerogels with increased compressive ε and intuitive representation of the mechanical property

$BSiTa_{0.2}$-PA has significant advantages over the reported high-performance aerogels, as shown in Table S5. Meanwhile, according to DTG curves, the pyrolysis of aerogels can be roughly divided into three stages (Fig. 3b). In the first stage, the degradation rate of $BSiTa_{0.2}$-PA is significantly lower than that of BSi-PA. In the second stage, the degradation rate of $BSiTa_{0.2}$-PA is also slightly lower than that of the sample without Ta. Since the second stage is the main pyrolysis stage, this stage is deconvolution and roughly divided into three pyrolysis peaks, as presented in Fig. 3c. It can be seen that the three pyrolysis peaks of $BSiTa_{0.2}$-PA are all higher than those of BSi-PA. It is possible because that the appropriate amount of Ta^{5+} coordination introduces Ta–O bridge into the cross-linking network of phenolic resin, where the Ta–O bond energy is up to 849 kJ mol^{-1} [32], much higher than the C–O and C–C chemical bonding energies. Furthermore, the composition analysis of the gas release of $BSiTa_{0.2}$-PA sample upon increasing temperature was conducted to understand the pyrolysis process by thermogravimetric infrared (TG-IR) in Fig. 3d. It can be seen that the release of H_2O is mainly

accompanied by the release of a few small carbon-containing molecules, such as CO_2, CO, and CH_4.

These results can be attributed to the following three reasons: (i) The solvothermal preparation process leads to the existence of a large number of unreacted end-hydroxyl group in the phenolic aerogel, which releases a large number of water molecules during the pyrolysis process; (ii) the cross-linking structure of $BSiTa_{0.2}$-PA hybrid phenolic aerogel is complex, in which the degree of cross-linking is large, and the relative content of the chain end segment in the cross-linking network is small, and thus, the initial decomposition temperature is higher; (iii) the hybrid elements, B, Si, Ta, and other hybrid elements, have strong "carbon fixation" ability and can undergo ceramic reaction with pyrolytic carbon in the heating process, and therefore, the char yield of $BSiTa_{0.2}$-PA is higher.

For thermal protection application, excellent mechanical robustness serves as a crucial assurance for aerogel to overcome deformation in extreme environments and facilitates the arbitrary shape preparation and subtractive manufacturing [33–35]. The compression performance of BSiTa-PA was tested and compared with the control sample (BSi-PA).

The typical compressive stress–strain ($\sigma - \varepsilon$) curves and modulus are shown in Fig. 3e, f and Table S2, in which BSiTa$_{0.2}$-PA shows the highest strength and modulus. Based on the classical deformation response of porous materials, the upward convex ring can be divided into three stages. In the first stage (the linear elastic deformation of BSiTa$_{0.2}$-PA ($\varepsilon < 5\%$)), the energy loss is relatively low with the corresponding less irreversible deformation, in which the slope of the stress–strain curve is used to derive Young's modulus. Next, after reaching the yield point, plastic deformation such as fracture of aerogels partial skeleton and joint failure occurs gradually. At last, the entire aerogel is densified.

To further demonstrate the compression flexibility of isotropic BSiTa$_{0.2}$-PA, uniaxial loading and unloading experiments with different strains were carried out, whose results are shown in Fig. 3f. It shows that as Ta^{5+} content increases, the compressive strength and modulus of the sample also display the tendency of rising up at the beginning then declining in late, in which the peak values occur in the case of BSiTa$_{0.2}$-PA sample, with the compressive strength ($\varepsilon = 30\%$) of 768.7 kPa and modulus of 7.1 MPa, respectively. The possible reason would be that Ta^{5+} can

form a stable chelated structure with phenolic organic structures, whose Ta–O bond energy is relatively higher [32]. However, with the excessive addition of Ta^{5+}, the mechanical properties decrease, indicating the stable chelated structure is disrupted. Since BSiTa$_{0.2}$-PA aerogel has the best mechanical strength and abundant micro-nano-structure, BSiTa$_{0.2}$-PA is chosen as the target materials in this work for the following performance investigation and microstructure analysis.

The thermal protection performance of the hybrid aerogels was assessed through static thermal insulation and dynamic ablative thermal insulation measurements, accompanied by a detailed analysis of the underlying mechanism via finite element method (FEM).

Firstly, the thermal conductivity of hybrid aerogel was investigated, as shown in Fig. 4a. Theoretically, the thermal conductivity of aerogel in air (λ_{total}) can be expressed as follows [36]:

$$\lambda_{\text{total}} = \lambda_{\text{conv}} + \lambda_{\text{rad}} + \lambda_{\text{air}} + \lambda_{\text{solid}} \tag{1}$$

where λ_{conv} represents heat convection; λ_{rad} is the contribution of thermal radiation; λ_{air} and λ_{solid} are thermal conductivity of gas phase and solid phase, respectively. Here,
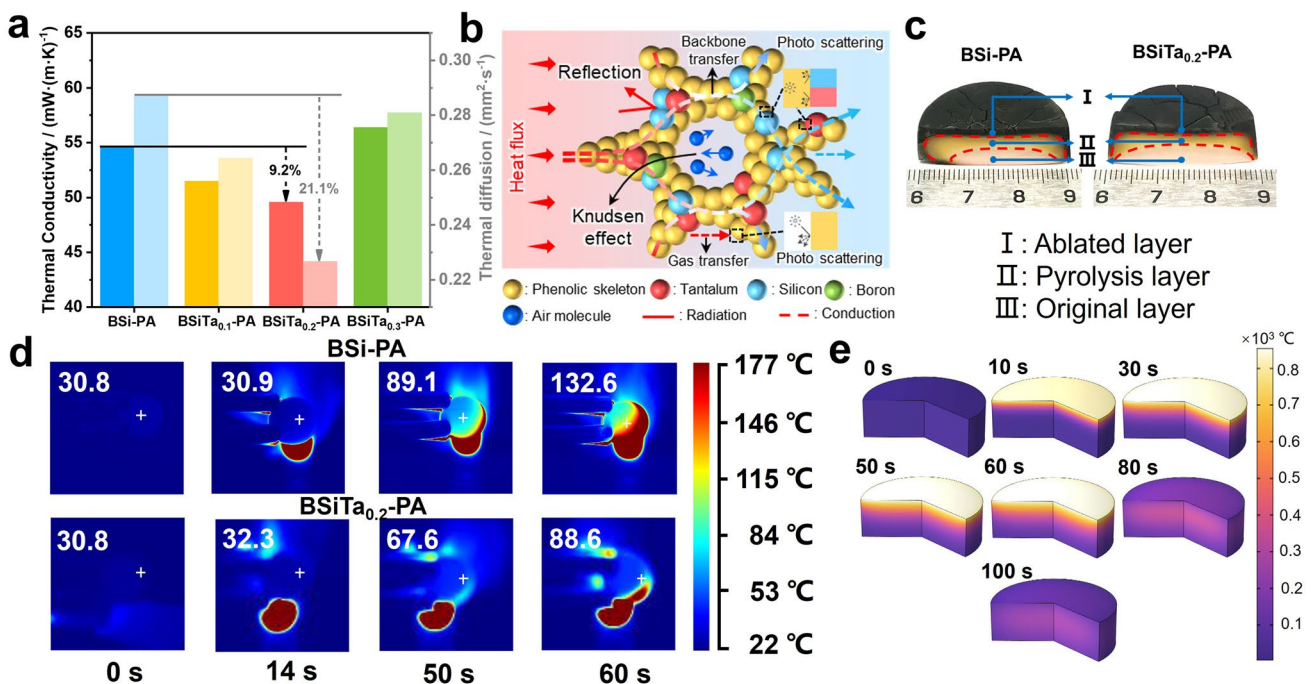
Fig. 4 Thermal insulation properties: **a** thermal conductivity and thermal diffusion of hybrid aerogels, **b** schematic illustration of the heat transfer process of the BSiTa$_{0.2}$-PA, **c** ablation cross sections of BSi-PA and BSiTa$_{0.2}$-PA, **d** infrared thermographic images of the BSi-PA and BSiTa$_{0.2}$-PA back side, **e** temperature field simulation cloud image of BSiTa$_{0.2}$-PA (0–60 s for ablation, 60–100 s for natural cooling)

λ_{conv} should be insignificant because the micro-/nanopore size of the prepared aerogels is much lower than the starting size of natural convection (> 1 mm); λ_{rad} should also be ignored because the in BSiTa$_{0.2}$-PA not only the infinite pore walls in the aerogel act as a heat shield, but also the silica in the skeleton is a highly effective anti-radiation material. In this case, therefore, the thermal conductivity of the hybrid aerogel is only related to λ_{solid} and λ_{air}. But since λ_{air} is suppressed and relatively stable due to the "Knudsen effect", λ_{solid} has the decisive effect on λ_{total}. The thermal conductivity property of the aerogels at room temperature shows that BSiTa$_{0.2}$-PA exhibits better thermal insulation features than others at the same bulk density, with thermal conductivity (λ) and thermal diffusion coefficient (α) as low as 49.6 mW m^{-1} K^{-1} and 0.22 mm^2 s^{-1} (Fig. 4a). The thermal insulation mechanism is shown in Fig. 4b. This good performance can be ascribed to the abundant multi-scale micro-/nanopore structure, including the intrinsic pores of the aerogel and the cage structure of POSS in its skeleton, low thermal conductivity of Ta–O and Si–O bond as excellent phonon barriers, greatly reducing λ_{solid} conduction. Additionally, due to the excellent thermal insulation and mechanical elasticity of BSiTa$_{0.2}$-PA, infrared stealth properties can be endowed as a bonus (Fig. S7c). For a more intuitively observation of this difference between static thermal insulation performances, the thermal insulation performance of the hybrid aerogels was tested on a static heat source at a constant temperature (130 °C) in Fig. S7a. The result shows that within 5 min, the surface temperature of BSiTa$_{0.2}$-PA always maintains a lower temperature compared to that of BSi-PA.

Furthermore, the butane torch flame was used to examine the dynamic ablative thermal insulation performance of hybrid aerogel. The variation of its back temperature was measured by infrared thermal imager, as shown in Fig. S7d. According to the pyrolysis state of the aerogel, the ablation cross section of the aerogel in Fig. 4c can be divided into three regions: (i) ablated layer, (ii) pyrolysis layer, and (iii) original layer. It can be intuitively seen that BSiTa$_{0.2}$-PA obviously retains more original layer. In Fig. 4d, after the ablation for 60 s, the central back temperature of BSiTa$_{0.2}$-PA is always lower than 90 °C, while the central back temperature of BSi-PA at 60 s has reached 132.6 °C. The reasons for this excellent thermal protection performance can be attributed to the following two aspects: (i) in the pyrolysis/ablation process of hybrid aerogel, the hybrid elements can undergo complex ceramic reactions, and the formed ceramic structure can act as an effective thermal barrier to resist further erosion by heat flow; (ii) due to the existence of POSS and metal–organic linkage (Ta–O)

with low thermal conductivity, proper content of POSS and Ta–O structure can effectively improve the thermal insulation performance of bulk aerogel.

Herein, a three-dimensional ablative model of hybrid aerogel was established by FEM, considering the mechanism of heat transfer/heat dissipation such as surface heat erosion, heat radiation and heat convection. Through theoretical simulation and calculation, the temperature field cloud image and back temperature variation rule of BSiTa$_{0.2}$-PA sample during the ablation process were obtained, as shown in Figs. 4e and S8, S9. Based on the comparison between the experimental data and the simulation results, it can be seen that the peak back temperature obtained by the FEM simulation is similar to the experimental results, and the simulated back temperature curve is basically consistent with the fitting curve of the experimental back temperature, so the theoretical calculation results are convincing. Thus, we can accurately obtain the temperature changes and location of the ablative surface, pyrolytic layer, and original material of the sample from the obtained temperature field, combined with the thermal stability features of the sample, so as to conduct subsequent microstructure analysis.

3.3 Ceramic/Carbon Structural Transformation and Efficient EMI Shielding Properties of Multi-Hybrid Carbon Aerogel

Ablation of thermal protection is usually divided into surface ablation and volumetric ablation, representing the removal of materials from heat-exposed surfaces and the decomposition of internal materials, respectively [37]. As a result, the portion that undergoes volumetric ablation internally usually forms a bulk carbon material, which maintains its structural integrity and confers additional functional properties. As mentioned in Sect. 3.2, in addition to the excellent thermal stability, the high aromatic ring packing density makes phenolic also have an excellent high-temperature shape retention, which is the reason that phenolic is often used as a precursor to carbon materials, especially hard carbon [13, 38].

Through volumetric ablation of BSiTa$_{0.2}$-PA in the gradient temperature range, the EMI shielding performance of its ablated aerogel monolith with different levels of carbonization/ceramization in the X-band (8.2–12.4 GHz) was analyzed (Fig. 5a–c and Table S4). As the ablation temperature increases, the absorption and reflection losses
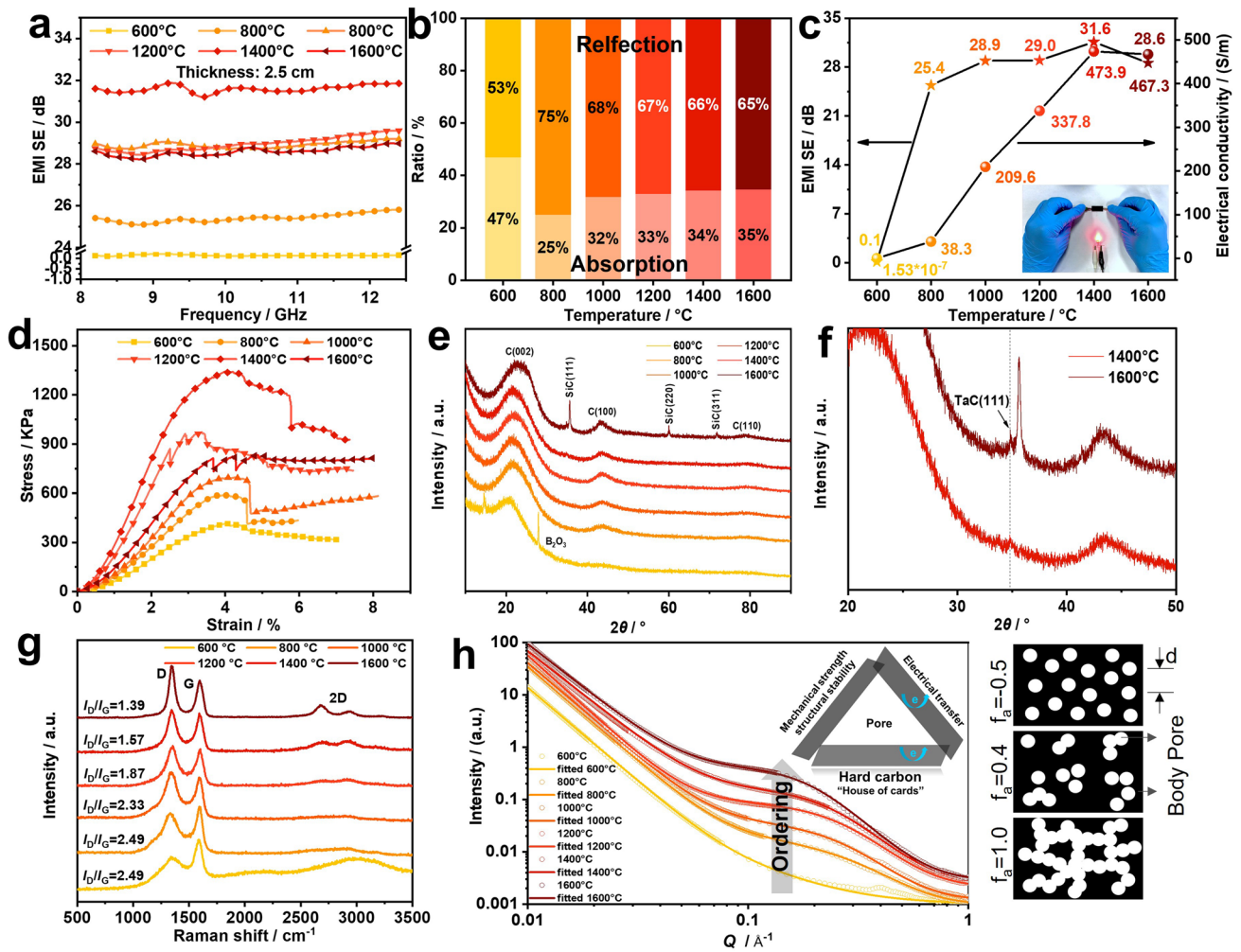
Fig. 5 EMI shielding and electrical conductivity performance: **a** EMI SE–Frequency curves for aerogels under different ablation temperature, **b** the absorption and reflection ratio of EMI SE, **c** average EMI SE and electrical conductivity of aerogels. Mechanical property: **d** compression $\sigma-\varepsilon$ curves of ablated aerogel. Ceramic/carbon/pore structure transformation analysis of different volumetric ablated aerogel: **e, f** XRD, **g** Raman spectra, **h** SAXS

are redistributed. When the ambient temperature reaches 1400 °C, the obtained aerogel has the best EMI shielding capability with an average efficiency of 31.6 dB, which can shield 99.9% of electromagnetic interference. By combining the TGA and electrical conductivity characteristics of BSiTa$_{0.2}$-PA, it can be seen that under a temperature of 600 °C, the sample has not been completely pyrolyzed; therefore, the existence of organic structure makes its electrical resistance larger, with an electrical conductivity of only 1.53×10^{-7} S m^{-1}. When the temperature is higher than 800 °C, the char yield of the sample gradually tends to be stable, accompanied with the electrical conductivity increases exponentially (reaches 473.9 S m^{-1} at 1400 °C),

which indicates that the carbon component in the aerogel forms a well-conductive structure. For stably practical application in EMI shielding, the mechanical strength of aerogel is crucial [39]. As shown in Fig. 5d and Table S3, with the increasing of ablation temperature, the skeleton strength of hybrid carbon aerogel exhibits the tendency of rising up at the beginning then declining in late, in which the peak specific modulus reaches 267.4 kN·m kg^{-1} at 1400 °C. When the heat treatment temperature further increases to 1600 °C, the specific modulus decreases to 147.7 kN·m kg^{-1}.

To explain the fine EMI shielding, ablative resistance and mechanical robustness of the obtained aerogel by high-temperature volumetric ablation, the microstructure of the

aerogel at different temperatures was analyzed by XRD, SAXS, XPS, Raman spectroscopy, MIP, and SEM. Figure 5e, f shows the XRD of BSiTa$_{0.2}$-PA samples pyrolyzed in the range of 600–1600 °C. It can be seen that these dominant peaks ascribed to (002), (100), and (110) reflections of graphite-like structure (with space group of $P6_3/mmc$) are obviously broad, which may be due to the small domain of graphite microcrystals and the existence of defects. With the increase of ablation temperature, these peaks turn to be shaper, in which the (002) peak gradually moves to a higher 2θ angle, indicating that the crystallinity of the sample is increasing (although the entire crystallinity level is low compared with graphite), with a decreasing interlay distance of carbon layers [40]. Meanwhile, sharp Bragg peaks appear in at 1600 °C, indexing to (111), (220), and (311) reflections from SiC (F_34m space group). An additional small fraction of sharp peak was observed at 2θ angle of around 34.8°, associated with a small amount of TaC ceramic crystal as shown in the enlarged region in Fig. 5f. Under 600 °C, two peaks at 14.7° and 27.9° appear, ascribed to B_2O_3. The structural evolution at various temperature is corroborated by the analysis of XPS and Gibbs free energy of thermochemical reactions (Fig. S10a–d).

According to the Raman spectra (Fig. 5g), the graphitization degree (I_D/I_G) of the carbon layer structure increases with the increasing temperature. When the ablation temperature reaches 1400 °C, the value of I_D/I_G goes to 1.57, and the 2D peak at 2500–3000 cm^{-1} is gradually remarkable, demonstrating the formation of the graphite structure. Since graphite microcrystals are effective carriers of electron transport, the degree of graphitization is positively correlated with the electrical conductivity [41]. Meanwhile, highly conductive TaC crystal appears at 1400 °C, further improving the electrical conductivity [42]. The increase in conductivity gives rise to a strong impedance mismatch, thus leading to more reflection losses [43]. In addition, with the increase of ablation temperature, the ceramic structure of aerogel gradually becomes stable, in which a large amount of heterogeneous interfaces between the graphite and SiOC amorphous composite ceramic, etc., formed at 1400 °C can produce a certain polarization loss and contribute to the EMI shielding performance [44].

The multiple reflections caused by the multi-scale pore structure in the aerogel can effectively enhance the interface polarization, to improve the absorption ability of electromagnetic interference [39, 45]. In Fig. S10e, f and Table S3,

the MIP results show that with the increase of the volumetric ablation temperature, the average macropore reaches the minimum value of 1291.6 nm when it reaches 1400 °C. In that case, the EMI shielding performance also peaks compared to cases at other temperature points. However, when the temperature further increases to 1600 °C, the average diameter of macropores increases, which may be because the Si-based ceramic vaporizes at this temperature point and overflow from the aerogel skeleton, generating part of the gas pore and resulting in the further expanding of the existing large pore.

Phenolic resins are usually an important source of hard carbon because of their inability to form fully cross-linked precursors in a semi-fluid state during pyrolysis [38]. This microstructure of hard carbon is a non-graphitic carbon material with tiny small (< 20 Å) graphite domains inside [46]. It is supposed to form many nanopores in the materials surrounded by small graphite domains (as shown in Fig. 5h) [47]. However, MIP and SEM are not adequate to evaluate the nano-scale pores especially the closed nanopores, and thereby SAXS has been performed to identify the nanopores including closed pores [48]. The details about theoretical models used for refining the SAXS intensity are presented in Supporting Information, to extract the pore size distribution and volume fraction of pores. The applied Teubner–Strey model gives the information of an average distance d between pores, the amphiphilic factor f_a as a disorder parameter and the average pore radius r [49]. The SAXS fitting results listed in Figs. 5h and S11 show that as increasing the ablation temperature (800–1600 °C), the pores feature of samples displays corresponding variations. The average pore radius r is less than 10 Å, confirming the nano-scale porous character in volumetric ablative samples, which turns to be smaller (from 8.64 to 4.63 Å) with the increasing temperature. The disorder parameter f_a decreases from ~0.72 to ~0.07 (at 1000–1600 °C), which is smaller than that for randomly spread globule shaped pores ($f_a = 0.4$), representing an increasing degree of short-range pore–pore ordering. In particular, the pore–pore distance d increases with the temperature from 1000 to 1600 °C and, however, is slightly higher in the sample at 800 °C. This exception is possibly due to the less-concentrated large pores with random distribution in the sample processed at 800 °C, which is consistent with its largest d, r and f_a values.

Based on the above microstructure analysis, we can draw a safe conclusion that the aerogel after ablation can turn to

be a carbon material with similar structure of hard carbon, which possesses a turbostratic structure (so called "house of cards") showing great advantages in mechanical strength and structural stability, and also make a contribution to the EMI shielding. With the further increase of temperature, some gas pores are generated due to the overflow of some hybrid element in aerogel, which leads to the weakening of skeleton strength. Although the degree of graphitization is further improved at 1600 °C, its compression modulus is still not stable at this stage.

4 Conclusions

In summary, to satisfy the more extreme complex thermal and electromagnetic environments in cosmic space, a new boron–silicon–tantalum ternary hybrid phenolic aerogel (BSiTa-PA) with excellent machinability, mechanical properties (39.4 kN·m kg^{-1}), superhydrophobic (> 150°), thermal insulation (49.6 mW m^{-1} K^{-1}), and ablative resistance properties was prepared. After extremely thermal erosion, the obtained carbon aerogel monolith demonstrates noteworthy EMI shielding performance with an efficiency of 31.6 dB at 1400 °C, accompanied by good load-carrying property with specific modulus of 272.8 kN·m kg^{-1}. An in-depth understanding of the microstructural evolution of the aerogel during volumetric ablation was found that the small graphite domains, good ceramic structures, and abundant nanopores during the ablation process, in conjunction with the pore structure inherent to aerogel, are the key reason for the excellent ablative resistance and electromagnetic shielding properties of the aerogel. The development of this convertible, multifunctional aerogel lays the foundation for the advancement of insulating materials in next-generation aerospace applications.

Declarations

Supplementary Information The online version contains supplementary material available at https://doi.org/10.1007/s40820-024-01409-1.

References

1. J. Guo, S. Fu, Y. Deng, X. Xu, S. Laima et al., Hypocrystalline ceramic aerogels for thermal insulation at extreme conditions. Nature **606**, 909–916 (2022). https://doi.org/10.1038/s41586-022-04784-0

2. M. Wu, H. Geng, Y. Hu, H. Ma, C. Yang et al., Superelastic graphene aerogel-based metamaterials. Nat. Commun. **13**, 4561 (2022). https://doi.org/10.1038/s41467-022-32200-8

3. F. Wu, P. Hu, F. Hu, Z. Tian, J. Tang et al., Multifunctional MXene/C aerogels for enhanced microwave absorption and thermal insulation. Nano-Micro Lett. **15**, 194 (2023). https://doi.org/10.1007/s40820-023-01158-7

4. Z.-M. Han, W.-B. Sun, K.-P. Yang, H.-B. Yang, Z.-X. Liu et al., An all-natural wood-inspired aerogel. Angew. Chem. Int. Ed. **62**(6), e202211099 (2023). https://doi.org/10.1002/anie.202211099

5. L. Su, S. Jia, J. Ren, X. Lu, S.-W. Guo et al., Strong yet flexible ceramic aerogel. Nat. Commun. **14**, 7057 (2023). https://doi.org/10.1038/s41467-023-42703-7

6. J. Zhang, J. Zheng, M. Gao, C. Xu, Y. Cheng et al., Nacre-mimetic nanocomposite aerogels with exceptional mechanical performance for thermal superinsulation at extreme conditions. Adv. Mater. **35**, e2300813 (2023). https://doi.org/10.1002/adma.202300813

7. V.A. Edlabadkar, S. Gorla, R.U. Soni, A.B.M.S.U. Doulah, J. Gloriod et al., Polybenzodiazine aerogels: all-nitrogen analogues of polybenzoxazines-synthesis, characterization, and high-yield conversion to nanoporous carbons. Chem. Mater. **35**, 432–446 (2023). https://doi.org/10.1021/acs.chemmater.2c02797

8. X. Li, R. Hu, Z. Xiong, D. Wang, Z. Zhang et al., Metal-organic gel leading to customized magnetic-coupling engineering in carbon aerogels for excellent radar stealth and thermal insulation performances. Nano-Micro Lett. **16**, 42 (2023). https://doi.org/10.1007/s40820-023-01255-7

9. X.-C. Lin, S.-L. Li, W.-X. Li, Z.-H. Wang, J.-Y. Zhang et al., Thermo-responsive self-ceramifiable robust aerogel with exceptional strengthening and thermal insulating performance at ultrahigh temperatures. Adv. Funct. Mater. **33**, 2214913 (2023). https://doi.org/10.1002/adfm.202214913

10. Y. Chen, Y. Yang, Y. Xiong, L. Zhang, W. Xu et al., Porous aerogel and sponge composites: assisted by novel nanomaterials for electromagnetic interference shielding. Nano Today **38**, 101204 (2021). https://doi.org/10.1016/j.nantod.2021.101204

11. L. Feng, P. Wei, Q. Song, J. Zhang, Q. Fu et al., Superelastic, highly conductive, superhydrophobic, and powerful electromagnetic shielding hybrid aerogels built from orthogonal graphene and boron nitride nanoribbons. ACS Nano **16**, 17049–17061 (2022). https://doi.org/10.1021/acsnano.2c07187

12. N.P. Padture, Advanced structural ceramics in aerospace propulsion. Nat. Mater. **15**, 804–809 (2016). https://doi.org/10.1038/nmat4687

13. J. Li, P. Guo, C. Hu, S. Pang, J. Ma et al., Fabrication of large aerogel-like carbon/carbon composites with excellent load-bearing capacity and thermal-insulating performance at 1800 °C. ACS Nano **16**, 6565–6577 (2022). https://doi.org/10.1021/acsnano.2c00943

14. P. Guo, J. Li, S. Pang, C. Hu, S. Tang et al., Ultralight carbon fiber felt reinforced monolithic carbon aerogel composites with excellent thermal insulation performance. Carbon **183**, 525–529 (2021). https://doi.org/10.1016/j.carbon.2021.07.027

15. Z. Yang, J. Li, X. Xu, S. Pang, C. Hu et al., Synthesis of monolithic carbon aerogels with high mechanical strength via ambient pressure drying without solvent exchange. J. Mater. Sci. Technol. **50**, 66–74 (2020). https://doi.org/10.1016/j.jmst.2020.02.013

16. X. Chang, F. Wu, X. Cheng, H. Zhang, L. He et al., Multiscale interpenetrated/interconnected network design confers all-carbon aerogels with unprecedented thermomechanical properties for thermal insulation under extreme environments. Adv. Mater. **36**, e2308519 (2024). https://doi.org/10.1002/adma.202308519

17. T. Xue, Y. Yang, D. Yu, Q. Wali, Z. Wang et al., 3D printed integrated gradient-conductive MXene/CNT/polyimide aerogel frames for electromagnetic interference shielding with ultra-low reflection. Nano-Micro Lett. **15**, 45 (2023). https://doi.org/10.1007/s40820-023-01017-5

18. Z. Niu, Y. Xin, L. Wang, S. Shen, X. Ma et al., Two birds with one stone: Construction of bifunctional-poss hybridized boron-silicon ceramicized phenolic composites and its ablation behavior. J. Mater. Sci. Technol. **141**, 199–208 (2023). https://doi.org/10.1016/j.jmst.2022.10.004

19. Z. Niu, B. Chen, S. Shen, H. Zhang, X. Ma et al., Zirconium chelated hybrid phenolic resin with enhanced thermal and ablation resistance properties for thermal insulation composites. Compos. Commun. **35**, 101284 (2022). https://doi.org/10.1016/j.coco.2022.101284

20. W. Wang, X. Jin, H. Huang, S. Hu, C. Wu et al., Thermal-insulation and ablation-resistance of Ti-Si binary modified carbon/phenolic nanocomposites for high-temperature thermal protection. Compos. A Appl. Sci. Manuf. **169**, 107528 (2023). https://doi.org/10.1016/j.compositesa.2023.107528

21. X. Jin, C. Liu, H. Huang, R. Pan, C. Wu et al., Multiscale, elastic, and low-density carbon fibre/siliconoxycarbide-phenolic interpenetrating aerogel nanocomposite for ablative thermal protection. Compos. B Eng. **245**, 110212 (2022). https://doi.org/10.1016/j.compositesb.2022.110212

22. H. Geng, Q.-Z. Zhong, J. Li, Z. Lin, J. Cui et al., Metal ion-directed functional metal-phenolic materials. Chem. Rev. **122**, 11432–11473 (2022). https://doi.org/10.1021/acs.chemrev.1c01042

23. X. Xu, Q. Zhang, M. Hao, Y. Hu, Z. Lin et al., Double-negative-index ceramic aerogels for thermal superinsulation. Science **363**, 723–727 (2019). https://doi.org/10.1126/science.aav7304

24. M. Zhu, G. Li, W. Gong, L. Yan, X. Zhang, Calcium-doped boron nitride aerogel enables infrared stealth at high temperature up to 1300 °C. Nano-Micro Lett. **14**, 18 (2021). https://doi.org/10.1007/s40820-021-00754-9

25. Q. Yuan, L. Yan, J. Tian, W. Ding, Z. Heng et al., *In situ* ceramization of nanoscale interface enables aerogel with thermal protection at 1950 °C. ACS Nano **18**, 3520–3530 (2024). https://doi.org/10.1021/acsnano.3c11129

26. Z. Qian, H. Cai, J. Cao, P. Wang, L. Li et al., 3D needle-punched carbon/quartz fabric reinforced nanoporous phenolic composites with co-optimized mechanics, insulation and ablation. Compos. Commun. **36**, 101393 (2022). https://doi.org/10.1016/j.coco.2022.101393

27. M. Natali, J.M. Kenny, L. Torre, Science and technology of polymeric ablative materials for thermal protection systems and propulsion devices: a review. Prog. Mater. Sci. **84**, 192–275 (2016). https://doi.org/10.1016/j.pmatsci.2016.08.003

28. Z. Niu, G. Li, X. Ma, S. Shen, Y. Xin et al., Synergetic effect of O-POSS and T-POSS to enhance ablative resistant of phenolic-based silica fiber composites via strong interphase strength and ceramic formation. Compos. A Appl. Sci. Manuf. **155**, 106855 (2022). https://doi.org/10.1016/j.compositesa.2022.106855

29. Y. Huang, H. Zhang, Z. Liu, C. Zhou, L. Yan et al., Pre-oxidized mesophase pitch modified phenolic composites with mosaic-structured char layers and excellent ablation resistance. Compos. B: Engin. **257**, 110691 (2023). https://doi.org/10.1016/j.compositesb.2023.110691

30. Z. Niu, G. Li, Y. Xin, X. Ma, C. Zhang et al., Enhanced thermal and anti-ablation properties of high-temperature resistant

reactive POSS modified boron phenolic resin. J. Appl. Polym. Sci. **139**, 52087 (2022). https://doi.org/10.1002/app.52087

31. W. Zhang, S. Hu, H. Li, T. Song, L. Jiang et al., Epoxidized vinyl silicone rubber-based flexible ablative material with low linear ablation rate. Compos. Commun. **40**, 101606 (2023). https://doi.org/10.1016/j.coco.2023.101606

32. B. Chu, S. Liu, L. You, D. Liu, T. Huang et al., Enhancing the cycling stability of Ni-rich $LiNi_{0.6}Co_{0.2}Mn_{0.2}O_2$ cathode at a high cutoff voltage with Ta doping. ACS Sustain. Chem. Eng. **8**, 3082–3090 (2020). https://doi.org/10.1021/acssuschemeng.9b05560

33. Z.-L. Yu, N. Yang, V. Apostolopoulou-Kalkavoura, B. Qin, Z.-Y. Ma et al., Fire-retardant and thermally insulating phenolic-silica aerogels. Angew. Chem. Int. Ed. **57**, 4538–4542 (2018). https://doi.org/10.1002/anie.201711717

34. Z.-L. Yu, Z.-Y. Ma, H.-X. Yao, B. Qin, Y.-C. Gao et al., Economical architected foamy aerogel coating for energy conservation and flame resistance. ACS Mater. Lett. **4**, 1453–1461 (2022). https://doi.org/10.1021/acsmaterialslett.2c00419

35. S. Zhao, W.J. Malfait, A. Demilecamps, Y. Zhang, S. Brunner et al., Strong, thermally superinsulating biopolymer–silica aerogel hybrids by cogelation of silicic acid with pectin. Angew. Chem. Int. Ed. **54**, 14282–14286 (2015). https://doi.org/10.1002/anie.201507328

36. H. Huang, X. Yan, X. Jin, C. Wu, Y. Pan et al., Flexible and interlocked quartz fibre reinforced dual polyimide network for high-temperature thermal protection. J. Mater. Chem. A **11**, 9931–9941 (2023). https://doi.org/10.1039/d3ta01413d

37. S. Shi, L. Li, J. Liang, S. Tang, Surface and volumetric ablation behaviors of SiFRP composites at high heating rates for thermal protection applications. Int. J. Heat Mass Transf. **102**, 1190–1198 (2016). https://doi.org/10.1016/j.ijheatmasstransfer.2016.06.085

38. Z.-L. Yu, B. Qin, Z.-Y. Ma, J. Huang, S.-C. Li et al., Superelastic hard carbon nanofiber aerogels. Adv. Mater. **31**, e1900651 (2019). https://doi.org/10.1002/adma.201900651

39. X. Ma, S. Liu, H. Luo, H. Guo, S. Jiang et al., MOF@wood derived ultrathin carbon composite film for electromagnetic interference shielding with effective absorption and electrothermal management. Adv. Funct. Mater. **34**, 2310126 (2024). https://doi.org/10.1002/adfm.202310126

40. Y. Morikawa, S.-I. Nishimura, R.-I. Hashimoto, M. Ohnuma, A. Yamada, Mechanism of sodium storage in hard carbon: an X-ray scattering analysis. Adv. Energy Mater. **10**, 1903176 (2020). https://doi.org/10.1002/aenm.201903176

41. C. Ding, L. Huang, X. Yan, F. Dunne, S. Hong et al., Robust, superelastic hard carbon with *in situ* ultrafine crystals. Adv. Funct. Mater. **30**, 1907486 (2020). https://doi.org/10.1002/adfm.201907486

42. H. Guo, F. Wang, H. Luo, Y. Li, Z. Lou et al., Flexible TaC/C electrospun non–woven fabrics with multiple spatial-scale conductive frameworks for efficient electromagnetic interference shielding. Compos. A Appl. Sci. Manuf. **151**, 106662 (2021). https://doi.org/10.1016/j.compositesa.2021.106662

43. R. Verma, P. Thakur, A. Chauhan, R. Jasrotia, A. Thakur, A review on MXene and its' composites for electromagnetic interference (EMI) shielding applications. Carbon **208**, 170–190 (2023). https://doi.org/10.1016/j.carbon.2023.03.050

44. W. Yang, D. Yang, H. Mei, L. Yao, S. Xiao et al., 3D printing of PDC-SiOC@SiC twins with high permittivity and electromagnetic interference shielding effectiveness. J. Eur. Ceram. Soc. **41**, 5437–5444 (2021). https://doi.org/10.1016/j.jeurceramsoc.2021.04.048

45. C. Liang, Z. Gu, Y. Zhang, Z. Ma, H. Qiu et al., Structural design strategies of polymer matrix composites for electromagnetic interference shielding: a review. Nano-Micro Lett. **13**, 181 (2021). https://doi.org/10.1007/s40820-021-00707-2

46. D. Chen, W. Zhang, K. Luo, Y. Song, Y. Zhong et al., Hard carbon for sodium storage: mechanism and optimization strategies toward commercialization. Energy Environ. Sci. **14**, 2244–2262 (2021). https://doi.org/10.1039/D0EE03916K

47. S. Alvin, D. Yoon, C. Chandra, H.S. Cahyadi, J.-H. Park et al., Revealing sodium ion storage mechanism in hard carbon. Carbon **145**, 67–81 (2019). https://doi.org/10.1016/j.carbon.2018.12.112

48. C.M. Jeffries, J. Ilavsky, A. Martel, S. Hinrichs, A. Meyer et al., Small-angle X-ray and neutron scattering. Nat. Rev. Meth. Primers **1**, 70 (2021). https://doi.org/10.1038/s43586-021-00064-9

49. D. Saurel, J. Segalini, M. Jauregui, A. Pendashteh, B. Daffos et al., A SAXS outlook on disordered carbonaceous materials for electrochemical energy storage. Energy Storage Mater. **21**, 162–173 (2019). https://doi.org/10.1016/j.ensm.2019.05.007